Electrochemical Atomic Force Microscopy Imaging of Redox-Immunomarked Proteins on Native Potyviruses: From Subparticle to Single-Protein Resolution

Laurent Nault,[†] Cécilia Taofifenua,[†] Agnès Anne,[*,†] Arnaud Chovin,[†] Christophe Demaille,[*,†] Jane Besong-Ndika,[‡,§] Daniela Cardinale,[‡] Noëlle Carette,[‡] Thierry Michon,[*,‡] and Jocelyne Walter[‡]

[†]Laboratoire d'Electrochimie Moléculaire, Université Paris Diderot, Sorbonne Paris Cité, Unité Mixte de Recherche Université, CNRS No 7591, Bâtiment Lavoisier, 15 rue Jean-Antoine de Baïf, 75205 Cedex 13 Paris, France, [‡]UMR 1332 Biologie du Fruit et Pathologie, INRA-Université Bordeaux 2, 71 av. Edouard Bourlaux, 20032-33882 Cedex Villenave d'Ornon, France, and [§]Department of Food and Environmental Sciences, University of Helsinki, Latokartanonkaari 11, FI-00014 Helsinki, Finland

ABSTRACT We show herein that electrochemical atomic force microscopy (AFM-SECM), operated in molecule touching (Mt) mode and combined with redox immunomarking, enables the *in situ* mapping of the distribution of proteins on individual virus particles and makes localization of individual viral proteins possible. Acquisition of a topography image allows isolated virus particles to be identified and structurally characterized, while simultaneous acquisition of a current image allows the sought after protein, marked by redox antibodies, to be selectively located. We concomitantly show that Mt/AFM-SECM, due to its single-particle resolution, can also uniquely reveal the way redox functionalization endowed to viral particles is distributed both statistically among the viruses and spatially over individual virus particles. This possibility makes Mt/AFM-SECM a unique tool for viral nanotechnology.

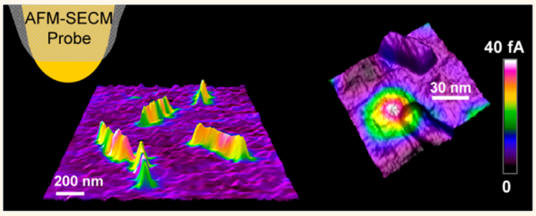

KEYWORDS: electrochemistry · electrochemical atomic force microscopy · functional nanosystems · virus nanocarriers · virus imaging · potyvirus

Viruses are fascinating natural nanomachines capable of performing complex tasks while displaying a minimalistic architecture.[1] They can infect all types of life forms, from bacteria to plants and animals, and as a result, their study is of paramount importance to fundamental biology, agronomy, and medicine. Moreover, in the last 20 years or so, viruses have been considered as functional nanoparticles for nanomedicine and nanotechnology applications. They have been used as nanovectors for targeted drug delivery or imaging,[2,3] nanocontainers for enzymatic catalysis,[4−6] or building blocks for complex assemblies with tuned functional or structural properties.[7,8] Hence, no matter the intended application, there is a need for high-resolution microscopy techniques enabling to image both native and modified (functionalized) virus particles. Typically, X-ray diffraction analysis and transmission electron microscopy (TEM) have been extensively used to "image" viruses.[9,10] X-ray diffraction and TEM offer unsurpassed resolution, approaching the atomic level, but as they are *ex situ* techniques, viruses have to be studied in the dry state, which may lead to structure alterations. Cryo-electron microscopy, a form of TEM where the sample is studied at cryogenic temperatures,[11] does allow 3D imaging of viruses in physiological environments (in vitreous ice). However, because images are actually reconstructions obtained by combining several digitized images of similar viral particles, they represent an *average* structure of the virus population.[12] As a result, the peculiarities of individual particles, which may be important, are averaged out. For all of these reasons, atomic force microscopy (AFM) has been proposed as an alternative technique for imaging viruses. AFM offers the multiple

* Address correspondence to
anne@univ-paris-diderot.fr,
demaille@univ-paris-diderot.fr,
tmichon@bordeaux.inra.fr.

Received for review November 20, 2014
and accepted April 23, 2015.

10.1021/acsnano.5b00952

advantages of enabling imaging of individual surface-immobilized viruses, with a resolution in the nanometer range, both *in situ* and with an actual 3D contrast.[13−15] The surface structures of various viral particles, may they be bacteriophages (*e.g.*, T4 phages),[16] plant viruses (*e.g.*, potato viruses),[17−19] or even human viruses (*e.g.*, simplex virus type 1),[20] have indeed been revealed by high-resolution AFM imaging. However, the applicability of AFM for characterizing *functionalized* viruses intended for nanotechnology applications is much more limited. The reason for this is that viral particles are typically endowed with specific functions *via* decoration with nano-objects or molecules such as enzymes[6] and photoactive[21−23] or redox groups,[24,25] which cannot be resolved in topography when attached to the virus shell because they are either too small or too soft for that.[14] As a result, the degree of labeling of the viruses and the actual function of these species cannot be assessed at the individual particle scale but only at the "ensemble" level (*i.e.*, as the average property of a virus containing solution). This is highly regrettable since the distribution of the functional moieties on single particles as well as the distribution of the functionalization over the whole population of particles cannot be determined and remains hidden. Hence, a technique allowing the *in situ* characterization of functionalized viruses at the individual virus particle scale is much needed. Ideally, isolated modified virus particles should be identified, their integrity checked, and their function probed. Hyphenated AFM techniques, such as AFM tip-enhanced Raman spectroscopy (TERS)[26,27] and AFM infrared spectroscopy (IR),[28,29] which were used to probe the secondary structure of virus proteins, could eventually be considered for this, but their implementation in liquid is extremely difficult. In that context, we intend to show here that AFM-SECM,[30−32] a technique combining AFM with scanning electrochemical microscopy (SECM) fulfills *all* of the above criteria and uniquely enables individual functional virus characterization.

SECM is a spatially resolved *in situ* technique using a microelectrode as a local probe to trigger and/or to monitor electrochemical processes occurring at surfaces.[33] A wealth of local surface processes and reactions,[34] including enzymatic reactions,[35] have been characterized by SECM, which can be seen as a *functional imaging* technique. Until relatively recently, the typical spatial resolution achieved in SECM was in the micron range, even though submicron resolution had been occasionally demonstrated.[36−38] As far as characterizing bio-objects was concerned, this was sufficient to probe processes occurring at the surface of life cells[39] but definitely not enough to resolve tiny nano-bio objects such as viruses. A notable and unique exception was the pioneering work of Bard *et al.*,[40] who imaged individual macromolecules, such as antibodies and hemocyanin, in a SECM-like configuration, but where the imaging medium was humid air and not an aqueous solution. Recent progress in nanoelectrode (tip) preparation[41−43] and the development of various tip-positioning techniques[44−46] have significantly improved the resolution of "regular" SECM down to a few tens of nanometers,[41−46] but the characterization of viruses by any SECM-related technique has not been reported. We propose here to use a high-resolution variant of AFM-SECM, which we introduced earlier,[47,48] and labeled Mt (mediator-tethered)/AFM-SECM,[49] for imaging individual virus particles.

The working principle of Mt/AFM-SECM is that a combined AFM-SECM microelectrode probe is used to electrochemically contact redox-labeled macromolecules immobilized on an electrode surface. We previously demonstrated that this original configuration allows the internal dynamics of nanometer-sized redox-labeled polyethylene glycol (PEG)[47,48] and DNA chains (oligonucleotides)[50] to be probed. We also showed that, when operated in imaging (tapping) mode, Mt/AFM-SECM permitted us to specifically map the surface distribution of redox-labeled macromolecules while simultaneously acquiring surface topography with nanometer resolution.[49] As an illustration of this unique dual-imaging capability and resolution, we recently were able to locate and to electrochemically address *individual* redox PEGylated gold nanoparticles on an electrode surface.[51] Finally, in earlier works, we also demonstrated that Mt/AFM-SECM could be successfully combined with redox immunomarking, which involves the use of antibodies decorated by redox (ferrocenylated) PEG chains, in order to *specifically* locate ∼100 nm sized antigen motifs on test surfaces.[52] We now demonstrate that this immunoredox Mt/AFM-SECM imaging configuration enables mapping the distribution of proteins on individual virus particles with *single*-protein resolution. We also show that Mt/AFM-SECM is a powerful tool for viral nanotechnology as it allows both the topography but also the *function*, here the redox function, of functionalized viruses to be characterized at the individual virus particle scale.

RESULTS AND DISCUSSION

Two types of virus particles are most often considered for nanotechnology applications: bacteriophages[53] and plant viruses.[7] These natural nanoparticles are harmless to humans; their supramolecular organization is rather simple, and they can be functionalized either genetically or chemically. Moreover, they can be produced in high amounts in good biosafety conditions. In the present work, we selected two filamentous plant viruses belonging to the Potyviridae family, genus *Potyvirus*: the lettuce mosaic virus (LMV) and the closely related potato virus A (PVA). Potyviruses are flexible rod-shaped particles (∼700−900 nm in length[54] and ∼10−15 nm in diameter[55]) formed by helical winding of identical 31 kDa coat proteins (CP) packing the viral genomic single-stranded RNA. Each helical pitch of about 3−4 nm is

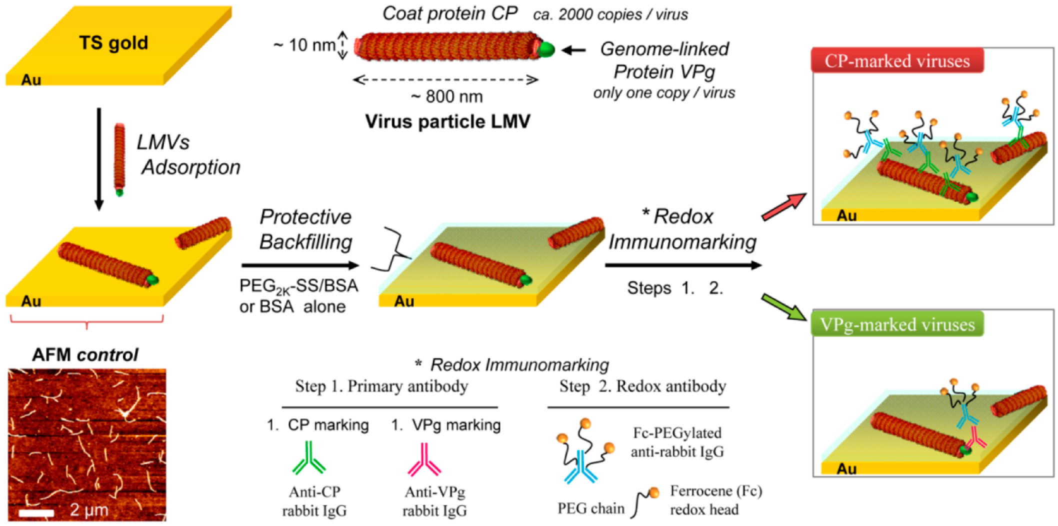

Figure 1. Schematic of the immobilization of LMV particles on a gold substrate and subsequent site-directed redox immunomarking. The AFM image shown in the lower left part of the figure is an actual 10 μm × 10 μm tapping mode topographic image of a control surface bearing a virus array, acquired in air and using a commercial AFM probe. Control surfaces were not engaged further in the assembly process but discarded after imaging. With the exception of this AFM control, all steps were performed in solution: the surface was never dried during the assembling process. Virus particle substrate coverage is derived by particle counting from the AFM control images: typically, $\gamma \sim 0.45$ individual virus particles/μm^2.

made of 9 CPs, giving approximately 1950–1985 CP units per particle (Figure 1).[56] Beside the CP, another viral protein, VPg (virus protein linked to the genome), is present in the particle. It is covalently linked to the 5′-end of the virus RNA and thus exists as a single copy located at the corresponding end of the virus particle (Figure 1).[57,58] It was postulated that a part of the VPg protrudes to the particle surface as it was specifically immunolabeled at one of the two virus ends together with two other viral proteins, namely, Hc-Pro[17] and CI.[59]

In order to be amenable to imaging by any local probe techniques, viruses, in general, have to be deposited, and ideally solidly anchored, onto a suitable planar substrate.[13,14] Such is also the case for potyviruses which have been previously successfully deposited on mica surfaces and imaged by AFM, mostly in air but also occasionally *in situ*.[17−19] In the present case, to enable Mt/AFM-SECM imaging, the substrate had to be conducting, and we thus turned to template-stripped gold.[60]

Immobilization and Redox Immunomarking of Lettuce Mosaic Virus on Gold Surfaces. In preliminary experiments, we used AFM imaging in air to assess simple spontaneous adsorption of LMV as a way of solidly anchoring this virus onto gold surfaces. Virus adsorption was carried out by leaving a freshly cleaved template-stripped gold surface in contact with a 50 μg/mL LMV solution in 10 mM pH 7.4 phosphate buffer for 10–20 min. After being rinsed copiously with buffer and then water, the surface was dried under N_2 for tapping mode AFM imaging. The topography images revealed the presence of a random array of viral particles (Figure 1, lower left corner). Most of the particles were individualized, many seemingly of similar length. Spider-like clusters, containing visibly a large number of viruses, were also sometimes observed (see Supporting Information Figure S1). The average individual viral particle coverage of the substrate, as determined from these images, was $\gamma = 0.2-0.5$ virus/μm^2. Higher coverage could be obtained for higher virus concentrations and adsorption time, but this latter coverage value was judged to be satisfying because it enabled visualization of many individual virus particles in few square micrometer images.

These results showed that simple adsorption does allow robust immobilization of LMV particles for tapping mode AFM imaging. Such was also the case for PVA, although instead of appearing as individual particles, this virus tended to form long "chains" on the gold surface (see Figure S9), a behavior already reported for PVA adsorbed onto mica.[18]

Beyond the problem of virus immobilization, implementation of immunoredox Mt/AFM-SECM imaging also requires that the virus is first marked by primary antibodies, specific to the sought after viral protein, which are then made electrochemically "visible" using secondary antibodies carrying imageable labels, redox ferrocene (Fc)-PEG chains in the present case. As it is done for routine immunomicroscopy techniques, such as immuno-TEM, we decided to carry out immunomarking after the virus was immobilized on the imaging substrate and not prior to it. Proceeding in this order greatly eases separation of the marked virus particles from the excess labeling antibodies. Importantly, since marking by antibodies requires that the biological structure of the virus is preserved, we made sure that the virus-bearing substrate was kept in buffer at all times (*i.e.*, never dried out). This "on surface" immunomarking method also imposes that nonspecific adsorption of the labeling antibodies onto the substrate is thoroughly blocked by a protective backfilling layer. In the present case, we observed that the best protection against nonspecific adsorption was achieved by self-assembly of a PEG_{2000}-disulfide chain layer complemented by adsorption of BSA (bovine serum albumin). Adsorption of BSA or self-assembly of PEG_{2000}-disulfide chains alone offered a good but somewhat lesser protection against nonspecific adsorption (see Methods section for details).

Two of the LMV viral proteins, the coat protein CP and the terminal protein VPg, were marked in separate experiments using, respectively, anti-CP- or anti-VPg-specific rabbit immunoglobulin gamma (IgG) as primary antibodies and anti-rabbit IgG labeled with Fc-PEG_{3400} chains as secondary antibodies (see Figure 1 and Methods). We previously produced and characterized such Fc-PEGylated antibodies, showing that in spite of the fact that they bear 5−10 Fc-PEG chains their molecular recognition capabilities remain intact.[52,53] In any case, we used sufficiently high antibody concentrations and recognition time so that the recognition reactions proceeded to completion (*i.e.*, marking was maximal; see Methods).

Redox CP immunomarking of LMV was evidenced at the "ensemble level" by recording a cyclic voltammogram (CV) at the substrate bearing the CP-marked virus particles. The CV displayed a weak but well-defined peak-shaped signal corresponding to the electrochemical response of the Fc heads.[51] Its integration yielded the total amount of Fc heads on the surface (see Figure S3). However, due to the presence of the spider-like virus clusters on the surface, which contained an impossible to evaluate number of LMV particles (see Figure S1), it was not possible to assign the amount of Fc heads detected to a reliable total number of virus particles. Hence, the *actual* number of Fc-PEG IgGs (or Fc-PEG chains) per virus could not be determined based on CV measurement but was ultimately estimated following a different strategy (see below).

Mt/AFM-SECM Imaging of CP-Marked LMV Particles. Gold surfaces bearing CP-marked LMV particles were imaged *in situ* (in 10 mM pH 7.4 phosphate buffer solution) in tapping mode Mt/AFM-SECM. To this aim, a homemade AFM-SECM tip was oscillated at its fundamental flexural resonance frequency (~2−3 kHz), biased at $E_{\text{tip}} = +0.3$ V/SCE and approached to the surface which was biased at $E_{\text{sub}} = 0.0$ V/SCE. Approach was stopped and raster imaging started when the tip oscillation was damped by ~10%. Acquired topography and tip current images, such as those respectively presented in Figure 2a and Figure 2b, were simultaneously recorded.

Examination of the topography image reveals five individual viral particles, which are ~900 nm long, ~85 nm wide, and 5−6 nm high. This apparent virus height is significantly lower than the known virus diameter (~13 nm).[55] Such an underestimation of height is an artifact commonly encountered when AFM is used to image soft nano-objects,[62] including antibodies[63] and viruses,[64,65] and is typically attributed to compression of the imaged object by the tip. Similarly, the apparent width of the virus particles is overestimated, as a result of the tip convolution effect common to all AFM-based techniques. In the case of a spherical AFM tip of radius R_{tip}, imaging a cylindrical

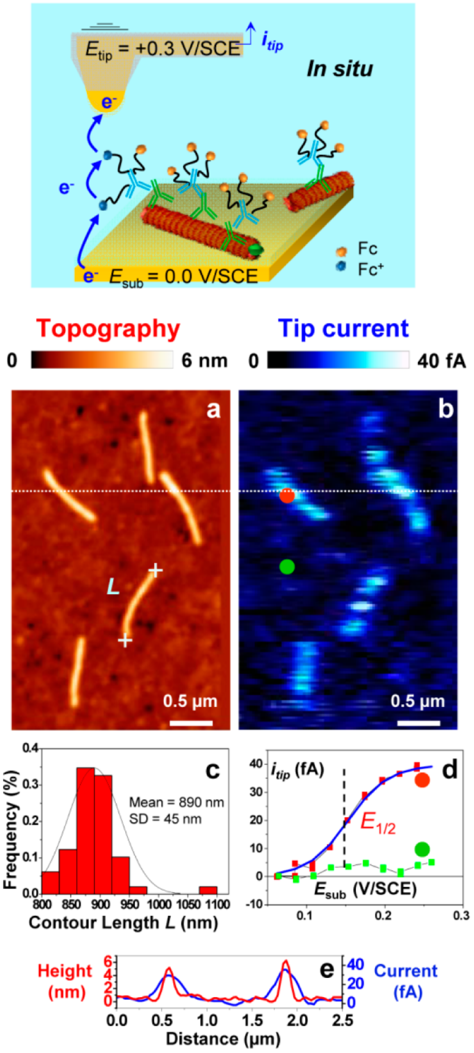

Figure 2. ***In situ*** **Mt/AFM-SECM tapping mode imaging of CP-marked LMV particles immobilized on a gold substrate. Top: Scheme of the redox cycling of the Fc heads borne by the Fc-PEGylated antibodies generating the tip current. Bottom: Simultaneously acquired topography (a) and tip current (b) images. The histogram in (c) shows the distribution of the contour length *L* of the virus particles as measured in (a). Shown in (d) is the dependence of the tip current i_{tip} with the substrate potential E_{sub}, with i_{tip} being measured either above a virus particle (red dot in (b) and (d)) or away from the viruses (green dot in (b) and (d)). Cross sections of the topography and current images along the dotted lines shown in (a) and (b) are plotted in (e), respectively, as red and blue traces. Tip potential for imaging $E_{\text{tip}} = 0.3$ V/SCE and substrate potential $E_{sub} = 0.0$ V/SCE. Imaging medium: 10 mM pH 7.4 phosphate buffer. The tip current image was first-order flattened.**

object of radius R_o, the apparent width of the object, w, is given by $w = 4(R_{tip}R_o)^{1/2}$ (see Supporting Information, Figure S11). Hence, considering that the radius of the combined AFM-SECM probes routinely used here fell in the 30−70 nm range, LMV is expected to appear as a 60−90 nm wide particle, in agreement with what can be measured in Figure 2a. However, because the virus length is much larger than the tip radius, the contour length of individual viruses, L, can be reasonably accurately measured from topography images, as shown in Figure 2a. We thus were able to sample the distribution of the LMV contour length over a relatively large population of a few tens of virus particles. The resulting distribution plot (histogram), presented in Figure 2c, shows that their contour length, L, is statistically distributed in the ~800−950 nm with an average value of 890 nm and a standard deviation of 45 nm (largely exceeding length measurement errors that we estimate to be in the order of ±10 nm). A similar kind of contour length distribution has previously been reported for the potyviruses PVA[18] and PVX.[19] Any further nanoscale analysis of the virus property has to take such dimensional diversity into account.

Turning now to the tip current image shown in Figure 2b, one can see that strings of current spots are detected at locations precisely corresponding to virus particles (see cross sections in Figure 2e). Actually, spots are detected all along the capsid of most virus particles, even though some viruses show only a few localized spots. Very few viruses displaying no current spots at all were occasionally observed (data not shown). It is also worth noticing that, as a benefit of the remarkable protective property of the PEG/BSA layer, we rarely observed spots in the "background" of the current images (*i.e.*, away from virus particles; see Methods).

The accurate tip-positioning capabilities of our AFM-SECM setup enable placing the tip at surface locations where a virus particle is seen and a current spot detected, for example, at the level of the red dot in Figure 2b. By incrementing E_{sub} step-by-step, it is then possible to monitor the substrate potential dependence of the tip current, i_{tip}. The resulting i_{tip} *versus* E_{sub} variation, reproduced in Figure 2d, is seen to be S-shaped and centered around a potential of approximately +0.15 V/SCE, which coincides with the standard potential of the Fc head of the Fc-PEG chains.[47,52] As also seen in Figure 2d, no such variation is observed when the tip is positioned away from any virus particle (*e.g.*, at the location of the green dot in Figure 2b). This result demonstrates that the current detected "above" the viruses is indeed due to the tip addressing Fc heads, which are alternatively oxidized at the tip and re-reduced at the substrate, as schematized at the top of Figure 2. Hence, the current images acquired here are to be interpreted as actual maps of the spatial distribution of the Fc-labeled antibodies, specifically bound to the anti-CP antibodies attached to the surface of individual virus particles. Consequently, the fact that, for most of the virus particles, current spots are recorded all along the capsid shows that the sought after protein (CP here) is present all along the virus. This result is a first demonstration of the possibility of using immunoredox Mt/AFM-SECM imaging for the *in situ* detection of viral proteins. Homogeneously "illuminated" objects could have been expected from the even distribution of CP molecules along the virus capsid, but virus particles appeared in the current image as strings of discrete spots. It is an intriguing finding that deserves further investigations. To get more insights into this phenomenon, zoomed-in images of virus particles, such as the one provided in Figure 3, were acquired.

From the topography image presented in Figure 3a and the corresponding cross sections taken along the two LMV particles shown (Figure 3d, red traces), one can see that the capsid appears essentially featureless (*i.e.*, "smooth"). At the opposite, the corresponding tip current image (Figure 3b) and cross sections (Figure 3d, blue and purple traces) show that well-defined current spots are indeed detected along the virus capsid. The individualization of the current spots can be better seen in the 3D current images shown in Figure 3c,e. We have observed these same characteristics for numerous LMV particles, albeit the number of spots per virus and the peak intensity of the spots varied greatly from one virus particle to the other (see Figure S4). These spots can be attributed to clusters of anti-CP/Fc-PEG IgG immunocomplexes bound to the virus capsid, and their differing intensities can be explained by the varying number of Fc heads, that is, of Fc-PEGylated IgGs, they contain. Indeed, since the Fc-PEGylated IgGs are polyclonal antibodies, several of them can bind to individual anti-CP antibodies. However, since the primary (anti-CP) and secondary (Fc-PEGylated) antibodies are similar in size, probably no more than ~3 IgG-PEG-Fc molecules can bind to each anti-CP antibody. It is also possible that each of the immunocomplex clusters contains more than one anti-CP antibody, which would further increase the number of Fc-PEGylated antibodies per spot. A qualitative indication about the cluster sizes can be obtained by observing that, in the current image, spots appear to be comparable in width (see Figure 3c); this shows that the size of the clusters was smaller than the tip radius.

Interestingly, comparing the topography image with the current image (Figure 3a,b) and corresponding cross sections (Figure 3d) reveals that the immunocomplex clusters decorating the virus particles are absolutely *not detected* in topography. This result falls in line with the already reported observation that IgGs cannot be clearly identified by AFM when bound to a virus.[14] This illustrates the limitations of topographic AFM for imaging soft objects placed on equally soft materials. On the contrary, the fact that antibody clusters are indeed detectable in the current images

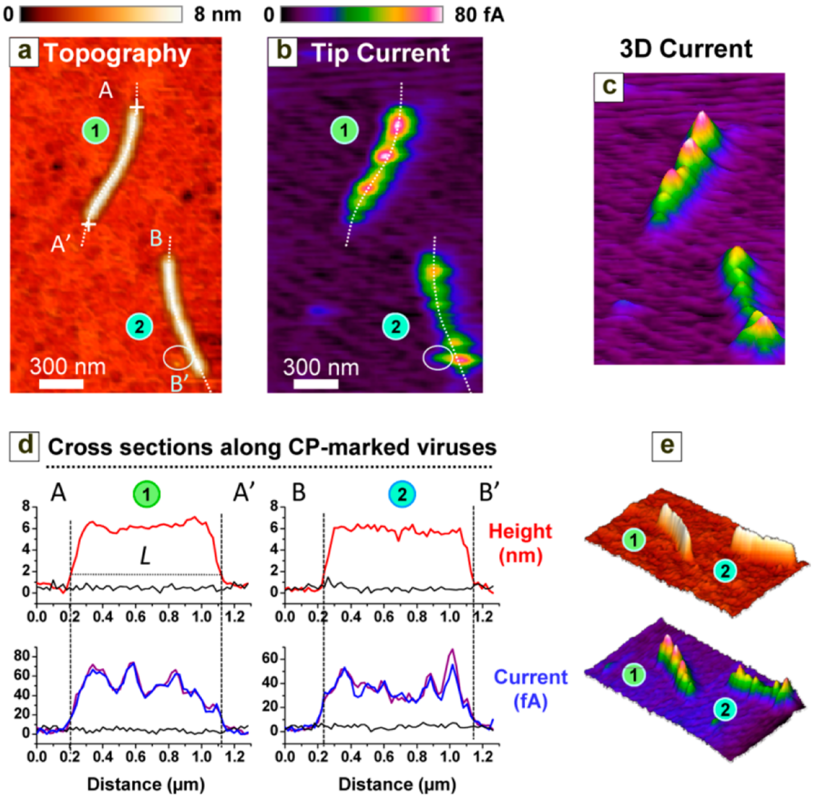

Figure 3. *In situ* Mt/AFM-SECM tapping mode imaging of CP-marked LMV particles immobilized on a gold substrate. Simultaneously acquired topography (a) and raw tip current (b) images. The tip current image is also presented in a 3D format in (c) to better show the string of current spots "borne" by the viruses. (d) Cross sections of the topography and current images taken along the viruses labeled (1) and (2) in (a) and (b). Curves in red are cross sections of the topography image (a); curves in blue and purple are cross sections of the trace (b) and retrace (not shown) current images, respectively. Cross sections taken away from the viruses are also shown as dark curves. (e) 3D tilted views of the topography and current images; $E_{tip} = 0.3$ V/SCE, $E_{sub} = 0.0$ V/SCE. Imaging medium: 10 mM pH 7.4 phosphate buffer.

demonstrates the usefulness of Mt/AFM-SECM as a new technique for mapping immunomarked proteins *on* virus particles.

The above results also indicate that Mt/AFM-SECM, due to its single-particle resolution, uniquely allows revealing the way redox functionalization is distributed not only among the viruses but also over individual viruses. This possibility motivated us to study further, that is, quantitatively and particle-by-particle, the extent and dispersion of the redox immunomarking of LMV.

Statistical Analysis of Mt/AFM-SECM Images: Revealing the Particle-to-Particle and Intraparticle Distribution of the Redox Functionalization of LMV. Twenty CP redox-immunomarked LMV particles were carefully imaged, and the number of current spots they "bore" together with their peak intensity was sampled. The resulting statistical data are shown in Figure 4.

Figure 4a is a histogram representing the distribution of the number of spots per virus. It shows that the large majority of the viruses "bore" from 4 to 10 spots, that is, immunocomplex clusters. The histogram in Figure 4b shows the distribution of the peak intensity of all of the current spots measured on all of the viruses sampled. The spot intensity is seen to closely follow a Gaussian distribution, hence, so did the number of Fc-PEG antibodies within the immunocomplex clusters. Taken together, these two results show that the degree of redox functionalization of the viruses did vary from one virus particle to another, partly because the number of immunocomplex clusters differed from one particle to another but mostly because the number of IgG-PEG-Fc per immunocomplex clusters varied to a large extent. In order to better visualize the actual dispersion of the degree of redox immunomarking of LMV, we summed up the intensities of the spots borne by each virus particle, probed, and plotted the resulting data in the histogram shown in Figure 4c. Recalling that in Mt/AFM-SECM the tip current generated by a redox-labeled object much smaller than the tip is simply proportional to the amount of redox heads it bears,[48] this histogram actually shows how redox labeling varied from one virus particle to the other. The corresponding average of these data, ~378 fA/virus, is thus proportional to the average degree of virus labeling. Examining Figure 4c, one can identify two dominant virus populations regarding their degree of redox marking compared to the average: one population, amounting to ~45% of the virus particles, was marked close to the average level, and another,

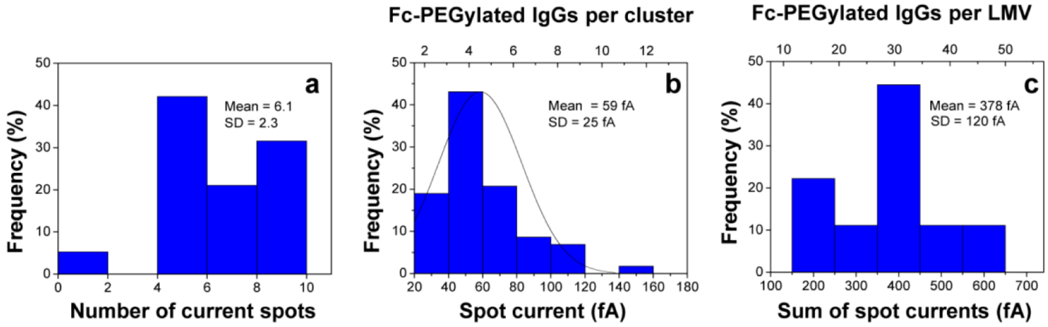

Figure 4. Statistical analysis of the redox immunomarking of 20 LMV particles as revealed by the current images. Histograms showing the distribution of the (a) number of current spots per virus. (b) Peak intensities of the current spots measured over all of the virus particles. (c) Summed up spot current intensities per virus. This latter histogram also represents qualitatively the dispersion of the degree of redox labeling among the virus particles.

amounting to ∼25% of the particles, was half as less marked. Globally, ∼20% of the virus particles were more labeled than average and 35% less.

Mt/AFM-SECM also enables studying the *spatial* distribution of redox labeling along individual virus particles. To carry out such a statistical analysis, the positions of the spots seen in the current images were reported on the topography image, and the distance x separating the center of each spot from one of the virus ends was carefully measured along the virus central axis (see scheme at the top of Figure 5).

In the process of collecting these data, we realized that one of the extremities of the virus particles always seemed to systematically bear less spots (*i.e.*, immunocomplex clusters) than the other. To quantify this phenomenon, we arbitrarily oriented the virus particles, ascribing the origin of the x axis to the extremity that bore the most spots. We then built a histogram of the cluster coordinates x normalized by the contour length of the corresponding virus particle (to account for the dispersion in virus length). This histogram, shown in Figure 5a, reveals that, whereas clusters are uniformly distributed on the central part of the viruses (from $x/L = 0.2$ to 0.9), they are indeed seldomly found at the virus extremity corresponding to $x/L = 0.9-1.0$. They are also slightly over-represented at the other extremity ($x/L = 0-0.2$). This result may seem surprising considering that the CP protein is uniformly present all along the virus capsid, but it falls in line with the fact that the molecular architecture of the virus is actually asymmetric by nature in that the two ends of the virus are made of different proteins. Hence, it is conceivable that the CP molecules neighboring one of the virus ends experience an environment that somehow disfavors their recognition by anti-CP antibodies. Pushing further the statistical analysis of the distribution of the immunocomplex clusters on the virus capsid, we also attempted to evaluate the regularity of cluster spacing along individual viruses. To this aim, we defined the regularity function $\psi_j = (x_j - x_0)(n - 1)/l$, where j is the cluster index, x_0 is the coordinate of the first cluster, n is the number of clusters, and l is the distance separating the first cluster from the last (*i.e.*, the extent of cluster coverage), and calculated ψ_j for each of the clusters of any given virus particle (see drawing in Figure 5). We then plotted ψ_j as a function of the cluster index, $j = 0$ to $n - 1$, and obtained scatter plots such as the one shown in Figure 5b (only nine virus particles are considered for clarity). One can see that all of the points collapse on a single line given by $\psi_j = j$. This result quantitatively shows that the spacing between the immunocomplex clusters along the virus particles tends to be surprisingly regular. Yet, because of the distribution in virus contour length (Figure 2c), this spacing obviously varied from one virus particle to the other, in the 90 to 230 nm range.

Finally, since Mt/AFM-SECM allows the topography and the current response of the *same* nano-object (virus particle) to be probed, we were able to seek cross-correlations between the position of any given immunocomplex cluster along the virus particles and the number of Fc-PEGylated antibodies it contains (as reflected by the spot intensity). To do this, each of the oriented virus particles were divided into ten 0.1L wide segments, and the intensity of the spots falling in each segment were averaged and plotted as a function of the segment position in Figure 5c. From this figure, it can be concluded that the immunocomplex clusters located along most of the virus length are composed of a similar number of Fc-PEG antibodies and that those located at the spot-depleted end of the virus (x/L = 0.8 to 1) contain significantly fewer Fc-PEGylated antibodies. Hence, depletion in immunocomplex clusters and a lower number of Fc-PEGylated antibodies per cluster at the depleted end combine to make redox labeling of the virus "asymmetric": one of the virus extremities is statistically less redox active than the other extremity and also the virus "body". To the best of our knowledge, it is the first time that the spatial distribution of a *functional property* (a redox function here) of individual modified virus particles is probed *in situ*.

We have no explanation for our observation that the immunocomplexes form regular chains of clusters along the LMV particles. Interestingly, we did not

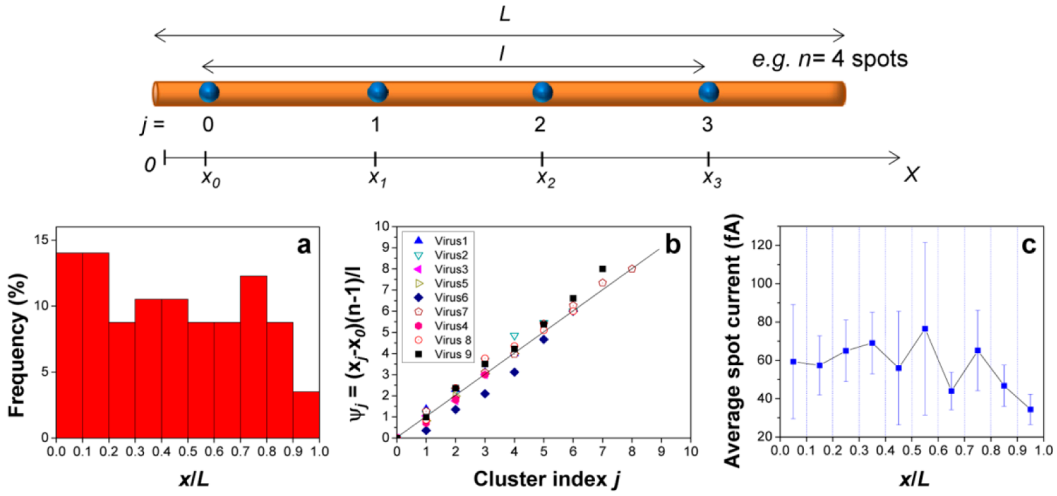

Figure 5. Statistical analysis of the spatial distribution of the immunoredox clusters along the capsid of LMV particles. Top: Schematic showing how the current spots (*i.e.*, clusters) are indexed (index *j*) and how their position relative to the virus end, x_j, is measured. Bottom: Histograms showing (a) spatial distribution of the clusters along the virus particles divided in ten 0.1*L* long segments. (b) Value of the regularity function ψ, defined as $\psi_j = (x_j - x_0)(n - 1)/l$ calculated for the clusters of nine virus particles (the black line is the variation predicted for perfectly regularly spaced clusters). (c) Cross-correlation of the spot intensities and their position along the virus particle divided in ten 0.1*L* long segments. The error bars are standard deviation of the spot current data.

observe this behavior for PVA, which was instead evenly labeled by the antibodies (see Figure S9). Such a labeling behavior is not necessarily detrimental for locating viral protein by immunoredox Mt/AFM-SECM imaging (see below), but is, however, important to reveal especially if immunolabeling is used to endow the virus particles with a redox function for nanotechnological applications. In such a case, being able to characterize the function of virus particles *in situ* (hence nondestructively) is also particularly important because it leaves open the possibility of further endowing the viruses with extra functionalities, such as enzymatic activity, after initial imaging.

Mt/AFM-SECM Imaging of VPg-Marked LMV Particles: Achieving Single-Protein Resolution. In order to further demonstrate the capability of Mt/AFM-SECM to map specific proteins on virus particles, we redox-immunomarked the terminal protein VPg of LMV. For this, we used polyclonal rabbit anti-VPg IgGs as primary antibodies and polyclonal anti-rabbit Fc-PEGylated IgGs as secondary antibodies. Simultaneously acquired Mt/AFM-SECM topography and current images of three VPg-marked LMV particles are shown in Figure 6 (see Supporting Information for extra images).

Images a and c of Figure 6A are the 3D rendering top view topography images of two individual virus particles, and images b and d in Figure 6A are the corresponding current images. These latter images are presented in a combined (overlaid) format, where the color scale representing the current contrast is mapped over the corresponding topography image. Examining these 3D overlay images reveals that a very clear current spot is selectively located at one end of each of the two virus particles. Importantly, in no case were current spots detected at both ends of the virus particles. The accurate location of the spots at the end of the viruses can be better assessed from the topography and current cross sections taken along the central axis of the viruses (panel A, lower part). One also sees in the current image that no current spots are found on the capsid of the viruses, even though a few spots are visible in the background. These background spots are Fc-PEGylated clusters (or isolated Fc-PEGylated IgGs) nonspecifically adsorbed on the gold surface; they were more numerous than in the case of CP-marking experiments because for VPg-marking a BSA protective layer was preferred over the PEG/BSA layer. This substitution was motivated by the fact that the PEG/BSA layer was observed to significantly decrease the yield of VPg marking (see below).

Most interestingly, as seen by comparing the topography and current images shown in Figure 6A, we observed that the current spots located at the end of the virus particles were systematically associated with a topography feature seemingly protruding from the virus end (see Supporting Information Figures S5 and S6). Two types of such features were observed: (i) either small objects (~50–70 nm in apparent width) only slightly protruding from the otherwise blunt virus extremity, such as seen in Figure 6, image a, and attributed to small immunocomplex clusters; or (ii) more rarely, ~150 nm long "tails" extending from the virus end, as is the case for the virus particle shown in Figure 6, image c. In this latter case, the spatial correspondence between the current spot and the "tail" can be visualized from the cross sections shown below image c in Figure 6. Overall, we observed that, for BSA-protected surfaces, ~15% of the virus particles were

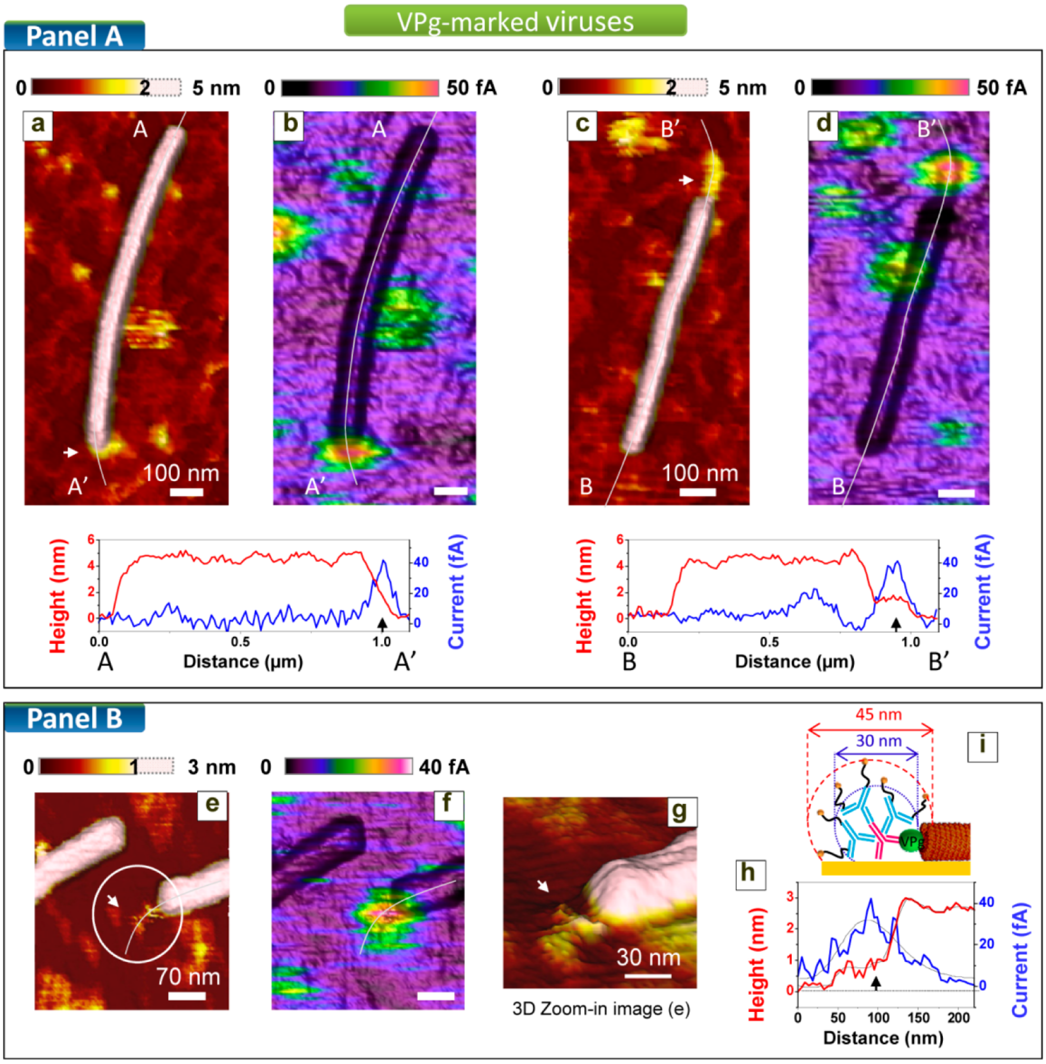

Figure 6. *In situ* Mt/AFM-SECM tapping mode imaging of VPg-marked LMV particles immobilized on a gold substrate. (A) (Top) Simultaneously acquired 3D rendering top view topography images (a,c) and tip current (b,d) images of two individual virus particles. (b,d) Color-coded contrast of the current images is overlaid to the corresponding topography images (a,c). (Bottom) Plots of the topography (red traces) and current (blue traces) cross sections taken along the lines shown, for the left plot in images (a,b) and for the right plot in images (c,d). (B) High-resolution 3D rendering top view topography image (e) and overlaid tip current image (f) of the extremities of two neighboring VPg-marked virus particles. The arrow in (e) points to a topography feature identified as an immunocomplex cluster better visible in the zoomed-in 3D tilted view shown in (g). (h) Plot of the topography (red trace) and current (blue trace) cross sections taken along the curved white lines shown in images (e,f). Black lines are smoothed original traces. (i) Schematic drawing (to scale) of the immunocomplex cluster formed at the VPg-exposing extremity of the virus.

marked at one of their extremities, whereas only ~5% were marked in the case of PEG/BSA-protected surfaces (see Supporting Information for details). These modest marking yields may be due to the limited accessibility of the VPg of surface-immobilized LMV to antibodies, a trend further amplified in the presence of a PEG layer.

Importantly, in control Mt/AFM-SECM experiments (reported in Supporting Information), where we used an "ineffective" anti-VPg antibody, no virus particles were found displaying the above-described characteristics typical of Vpg-marked viruses, that is, a topography feature protruding from the virus extremity correlated with a current spot at the same location. At the opposite, both ends of the viruses appeared to be systematically blunt.

The above results demonstrate the specific redox immunomarking of VPg and selective detection by Mt/AFM-SECM. Furthermore, since only a single copy of the VPg protein is displayed per LMV, we can confidently state that, by successfully imaging VPg-marked viruses, we demonstrated here the capability of Mt/AFM-SECM for locating individual viral protein molecules.

Yet, it is clear that the immunocomplex clusters identified at the virus ends are probably composed of several primary and secondary antibodies. In order to get insights into the structure and composition of these clusters, a particularly sharp AFM-SECM probe (apparent radius ~25 nm) was used to further image VPg-labeled viruses. The resulting high-resolution topography and overlaid current/topography images of the extremities of two neighboring virus particles are presented in Figure 6B, images e and f. One can see from these images that the end of the top virus is not associated with any visible feature neither in topography nor in current because it corresponds to the non-VPg-containing extremity of this particular virus. At the opposite, a small object, indicated by an arrow in image e (Figure 6B) and in the zoomed-in 3D tilted view shown in image g (Figure 6B), is visible at the end of the lower virus particle. As shown in image f, this object is associated with a clear current spot and is thus attributed to an immunocomplex cluster. Topography and current cross sections taken along this immunocomplex cluster, following the curved line shown in images e and f in Figure 6B, are displayed in image g. These cross sections allow us to measure the apparent size of the cluster; in topography, it appears as a ~65 nm sized object located exactly at the foot of the virus and in the current as a 100 nm wide rounded spot. Once corrected from the tip convolution effect, these apparent sizes translate into estimated actual imaged object diameters of ~22 and ~54 nm. These small diameters, approaching macromolecular dimensions, indicate that the immunoredox cluster located at the virus end is composed of very few antibodies. Indeed, considering their respective molecular weights, it seems unlikely that VPg (22 kDa)[66] can accommodate more than ~1 primary antibody (150 kDa). The fact that VPg may only partially protrude from the virus, and that the virus is adsorbed, may also contribute to sterically limit the accessibility of VPg to primary antibodies and, as a result, also limit the number of secondary antibodies in the immunocomplex cluster. This has already been observed in immuno-TEM experiments, where no more than 2 bulky gold-labeled secondary antibodies were seen to bind to the VPg-displaying end of potyviruses adsorbed on carbon grids.[58] The overall structure of the immunocomplex decorating the VPg can be coarsely evaluated on the basis of the simple 2D model presented in image i of Figure 6B. This model assumes that a maximum of three Fc-PEGylated antibodies can bind to the anti-VPg antibody. It is drawn to scale taking into account the actual sizes of the virus, of the antibodies (~15 nm),[67] and the "effective" ~10 nm length of the Fc-PEG chains.[51] It predicts that the antibodies occupy a roughly spherical volume of ~30 nm diameter, and that the elastically mobile Fc heads can be found in a spherical domain of ~45 nm diameter at the virus end. This simple model approximately reproduces the actual sizes of the immunocomplex cluster as estimated above from the topography and current images. It also allows us to visualize the reason why the current spots were systematically observed to be wider than the topography signature of the redox immunocomplexes: at the ~10 nm resolution attained, it is possible to sense the enlargement of the current spots due to the length of the Fc-PEG chains, whereas, as we already showed,[51] the PEG chains are too flexible to be probed in topography. Finally, it is also worth mentioning that the immunocomplex cluster as a whole probably does display some degree of elasticity (likely due to hinge motion of the IgG domains). Indeed, it regularly appeared as a "fuzzy" rather than a solid object on topography images (such is respectively the case in images e and a in Figure 6). This effect may also contribute to an underestimation of the cluster size as measured from the topography images. Having a reasonable idea of the structure of the immunocomplex cluster bound to VPg, we attempted to quantitatively analyze the current signal associated with it. In the present work, we observed that the intensity of the current spots resulting from the VPg labeling of LMV systematically fell in the ~15–40 fA range. Assuming that the maximum spot intensity of 40 fA, which we frequently measured (see Figure 6), corresponds to the maximum number of secondary antibodies in the immunocomplex cluster, and setting, as above, this number to ~3, we can derive a characteristic intensity of ~13 fA per IgG-PEG-Fc.

This characteristic value is of particular interest since it allows a reassessment of the CP-labeled virus data, to tentatively rescale the distribution plots in Figure 4 in terms of the number of Fc-PEGylated IgGs per CP-labeled virus particle. This yields an average number of IgG-PEG-Fc per virus of ~30 which, considering there are 5–10 Fc-PEG chains per antibody, leads to a coverage of 150–300 Fc heads per CP-marked LMV.

CONCLUSION

In this work, we demonstrated that immunoredox Mt/AFM-SECM imaging enables the *in situ* mapping of the distribution of proteins on individual virus particles. Acquisition of a topography image allows isolated virus particles to be identified and structurally characterized, while simultaneous acquisition of a current image allows the sought after protein, marked by redox antibodies, to be *selectively* located. The current detection sensitivity (~10 fA) and spatial resolution (~10 nm) achieved here are such that single-protein molecules (VPg) could be detected and located at the extremity of isolated viruses. Even though single molecules have already been detected by SECM,[68–70] this is the first time, to the best of our knowledge, that individual (macro) molecules have been imaged under *in situ* conditions using a SECM-based microscopy technique.

We concomitantly demonstrated that Mt/AFM-SECM, due to its single-particle resolution, can also uniquely reveal the way redox functionalization, here endowed to viral particles *via* redox antibodies, is distributed both *statistically* among the viruses and *spatially* over individual viruses. This possibility potentially makes Mt/AFM-SECM a versatile tool in the field of viral nanotechnology, where redox-functionalized viruses, intended as multiple electron reservoirs, have been produced (*via* chemical functionalization) but were so far only characterized at the "ensemble" level.[24,25]

METHODS

Biological Material. *Virus Particles.* Lettuce mosaic virus and potato virus A were prepared according to a previously published procedure,[59] modified as follows. Typically, 1 g of leaf material from previously infected plants (Lettuce mosaic virus, AF199 isolate) was grinded with 10 mM phosphate buffer, pH 7.0 (tissue-to-maceration ratio (W/v) of 1:5), and 0.1 g of carborundum (silicon carbide). Leaves from 75 young (10 cm high) *Nicotiana benthamiana* plants were softly rubbed with this preparation (carborundum particles induce small wounds on the leaf surface and facilitate virus penetration). All plants were grown in confined green house facilities under controlled light, moisture, and temperature conditions. After 25 days, 300 g of symptomatic leaves was homogenized in cold 0.1 M phosphate buffer pH 8, containing 0.15% 2-mercaptoethanol and 0.01 M EDTA (1 g leaves/2 mL buffer). Plant debris was spun down at 7000*g* for 20 min. After filtration through two layers of cheese cloth, Triton X-100 was added to the supernatant (final concentration 3%, v/v) and gently stirred at 4 °C for 3 h. The remaining insoluble material was spun down at 12 000*g* for 10 min. Virus particles were precipitated overnight by addition of PEG_{6000} (40 g/L of supernatant) and 0.2 M NaCl under gentle stirring at 4 °C in the dark. Virus particles were recovered by centrifugation at 12 000*g* for 20 min. The virus pellet was suspended in 1/10th of the starting supernatant in cold phosphate buffer 0.1 M, pH 8, containing 1% Triton X-100. This extract was centrifuged at 160 000*g* for 1 h at 4 °C. The pellet was gently suspended overnight at 4 °C in 0.1 M phosphate, pH 8 (5 mL for 100 g of starting leaves). Ultracentrifuge tubes (Beckman rotor SW 41 Tl, 13 mL vol) were filled with 5 mL of 30% sucrose in 0.1 M phosphate buffer pH 8. The virus suspension (2 mL per tube) was gently layered on the top of this sucrose cushion and centrifuged at 150 000*g* for 3 h at 4 °C. The pellet containing the virus particles was gently suspended overnight at 4 °C in 2 mL of 0.1 M phosphate buffer pH 8. The virus particles obtained were purified through a 5−40% discontinuous sucrose gradient as follows: centrifugation tubes (Beckman rotor SW 41 TI, 13 mL vol) were filled with sucrose solutions in phosphate buffer; from bottom to top, 1.5 mL 40%, 3 mL 30%, 3 mL 15%, 1.5 mL 5%. A volume of 0.5 to 1 mL of virus suspension was carefully layered on the top of the gradient. The virus preparation was centrifuged at 80 000*g* at 4 °C for 1 h. The pellet was suspended in the minimum amount of phosphate buffer (0.1 M) pH 8. The virus suspension was quantified by absorption spectrometry ($\varepsilon_{0.1\%}^{260\text{nm}} = 2.6$). Aliquots of 200 μL of virus (5−6 mg/mL) were stored at −80 °C. The characterization of one of these preparations is shown in Figure S10.

Primary and Secondary Unlabeled Antibodies. Anti-VPg rabbit polyclonal antibodies (pAB) from LMV were raised against a recombinant form of VPg produced in *E. coli*. The specificity of these antibodies was assessed by Western blot (Figure S11). LMV anti-CP and PVA anti-CP pAB were obtained from Dr. Hervé Lot (INRA Avignon, France) and Pr. Kristiina Mäkinen (Univ. Helsinki), respectively. The secondary polyclonal goat anti-rabbit IgGs and BSA (IgG-free grade) were from Jackson ImmunoResearch Laboratories.

Chemicals. A previously described home-synthesized heterobifunctional polyethylene glycol derivative NHS-PEG_{3400}-Fc (average number of OCH_2CH_2 monomer units 79), containing a redox ferrocene ethyl unit (Fc) at one end and an amine-reactive *N*-hydroxysuccinimide (NHS) ester at the other end, was used for Fc-PEGylation of the goat anti-rabbit antibodies.[71] The linear methoxy-terminated PEG_{2000} disulfide (PEG_{2K}-SS) molecule used for protective backfilling was custom-synthesized as described elsewhere.[52] Glutaraldehyde (EM grade), used as a fixative, was from Polysciences, Inc.

All other chemicals and solvents were analytical grade and used without further purification. All aqueous solutions were made with double-deionized water (18.2 MΩ·cm resistivity, TKA Micro-Pure UV). The same 10 mM pH 7.4 phosphate buffer solution was used to prepare the PEG_{2000} disulfide, BSA, antibody, and virus solutions. In order to prevent nonspecific adsorption, all of the antibody solutions contained 0.1% BSA and 0.1% Tween 20 (w/w), and 0.1% sodium azide was added as a preservative to all antibody solutions.

Preparation of the Fc-PEGylated IgGs. Attachment of Fc-PEG chains to goat anti-rabbit IgGs was carried out by reacting the NHS-activated ester of the home-synthesized NHS-PEG_{3400}-Fc chains with the amino groups of the IgG species, following a previously described procedure.[52,61]

Preparation of the Gold Surfaces. Flat gold surfaces were produced by template-stripping of a 200 nm thick gold layer deposited on mica,[60] as previously described.[51]

Adsorption of LMV on Gold and Redox Immunomarking. *Virus Adsorption.* The freshly peeled gold surface was immersed in the phosphate buffer solution containing LMV or PVA viruses at 50 μg/mL. After 10−20 min adsorption time, the surface was rinsed and left for 20 min in buffer for desorption of any weakly bound material.

Protective Backfilling Treatment. The surface was then backfilled either by a mixed PEG/BSA layer or a simple BSA layer. In the former case the surface was immersed in a 0.7 mM solution of PEG_{2000}-disulfide for 2 h followed by immersion in a 1 mg/mL BSA solution for 1 h. In the latter case, the surface was solely immersed in the BSA solution. The PEG/BSA layer displayed superior protective performances since almost no nonspecifically adsorbed Fc-PEGylated clusters could be detected in the current images (see Figure 2 and Figure 3). Actually, about one nonspecifically adsorbed Fc-PEGylated cluster could be seen per 10 μm^2 (representing 1/100000th of surface saturation by a 10 nm sized molecule). Protection by simple BSA adsorption was much less effective since as much ~40 nonspecifically adsorbed Fc-PEGylated clusters could be seen per 10 μm^2 (representing 1/2500th of saturation). Yet simple BSA protection was preferred for VPg-marking experiments since PEG/BSA protection tended to limit recognition of VPg by the antibodies.

Virus Marking by Antibodies. The surface was left in contact with a 5 μg/mL solution of polyclonal rabbit anti-CP (or anti-VPg) antibodies for 1 h. After being thoroughly rinsed, the surface was then left overnight in contact with a 20 μg/mL solution of polyclonal anti-rabbit Fc-PEGylated antibodies.

Fixation by Glutaraldehyde. Just before *in situ* Mt/AFM-SECM imaging, the surface was immersed in a 1% glutaraldehyde solution prepared in 10 mM pH 7.4 phosphate buffer and left to react for 15 min. This treatment hardens the viral structure and facilitates AFM imaging of viruses in liquid.[14,72] Unless otherwise stated, the samples were kept in phosphate buffer solution during all of their preparation and imaging. Surfaces were stored at room temperature, covered by phosphate buffer containing 0.1% sodium azide, and placed in a water-saturated atmosphere. This atmosphere was either air for BSA-protected surfaces or argon for PEG/BSA-protected surfaces (to preserve the PEG layer from oxidation).

Fabrication of the Combined AFM-SECM Tips. The tips were hand-fabricated according to a procedure adapted from literature[73] and largely detailed elsewhere.[74] Briefly, a 60 μm diameter gold wire was flattened, and its extremity was successively bent and etched to obtain a flexible cantilever bearing a conical tip with a spherical apex in the 20−100 nm range in radius (depending on the etching conditions).[51] The tip was fully insulated by deposition of an electrophoretic paint and glued onto an AFM chip. The apex was selectively exposed in order to act as a current-sensing nanoelectrode. The apparent radius of each tip was evaluated *in situ* by monitoring the width of the viruses, as measured from topography images, and using the equation relating the apparent size of a cylindrical object imaged in AFM to its actual diameter and to the tip radius (see Figure S11). The same tip could be used for several experiments in a row; tip fouling was rarely observed. However, we did notice that the tips tended to wear off slightly (their apparent radius tended to increase) but only after many hours of cumulated imaging time.

AFM and AFM-SECM Experiments. The AFM and Mt/AFM-SECM images were acquired using a JPK Nanowizard II microscope. In order to be operable in AFM-SECM mode, this microscope was modified according to specifications previously defined in our laboratory for another AFM system.[51] The standard JPK electrochemical liquid cell contained 900 μL of filtered pH 7.4 10 mM buffer solution and was equipped with a platinum wire as a counter electrode and a micro-Ag/AgCl reference electrode. All potentials in this work are reported *versus* the KCl saturated calomel electrode reference SCE (for easier comparison to biological redox scale +240 mV *vs* SHE).[75] A new generation of homemade bipotentiostat was used to control independently the potential applied to the substrate and to the electrochemical tip. Cyclic voltammograms could be recorded at the substrate while maintaining a constant bias at the tip. For the tip and substrate current acquisitions, high (0.8 pA/V) and low (10 μA/V) gain current measuring circuits were used. The tip current signal was passed through a 10 Hz low-pass analogue filter. Slow enough image scan rates (0.2−0.3 Hz) were used to avoid distortion of the current image by the filter. The substrate potential was generated by the JPK controller and the tip potential by the internal generator of the bipotentiostat. The tip−current data were corrected from the nonspecific leakage current resulting from the imperfect insulation of the connecting wires. This current is nonspecific and independent of the tip-to-substrate distance. Postacquisition processing of the current images was kept minimal. It consisted of first-order flattening followed by light Gaussian filtering. These processing steps did not significantly distort the current data as can be seen from Figure S10. Nevertheless, filtering was only applied for rendering purposes, and all current measurements were made on raw or flattened-only images. Images shown in text were processed using the WSxM software.[76]

Conflict of Interest: The authors declare no competing financial interest.

Acknowledgment. The authors acknowledge the support of the French Agence Nationale de la Recherche (ANR) under reference ANR-09-PIRI-0005 ("Cascade" project), ANR-09-CP2N ("Viruscaf" project), Academy of Finland (decision no. 1134684) for the J.B.-N. grant, and of the mission for interdisciplinarity of CNRS ("Nano" challenge program). The authors thank K. Mäkinen for fruitful discussions and for providing PVA CP antibodies.

Supporting Information Available: Additional figures for CP-marked LMV and comparison with CP-marked PVA. VPg-marked LMV, with extra images and control experiments data. The Supporting Information is available free of charge on the ACS Publications website at DOI: 10.1021/acsnano.5b00952.

Note Added after ASAP Publication: This paper was published ASAP on April 29, 2015. The caption for Figure S7 in the Supporting Information was corrected and the revised version was reposted on May 26, 2015.

REFERENCES AND NOTES

1. Flint, S. J.; Racaniello, V. R.; Enquist, L. W.; Skalka, A. M. *Principles of Virology*, 3rd ed.; ASM Press: Washington, DC, 2009; Vol. I Molecular Biology.
2. Steinmetz, N. F. Viral Nanoparticles as Platforms for Next-Generation Therapeutics and Imaging Devices. *Nanomedicine* **2010**, *6*, 634–641.
3. Carrico, Z. M.; Farkas, M. E.; Zhou, Y.; Hsiao, S. C.; Marks, J. D.; Chokhawala, H.; Clark, D. S.; Francis, M. B. N-Terminal Labeling of Filamentous Phage To Create Cancer Marker Imaging Agents. *ACS Nano* **2012**, *6*, 6675–6680.
4. Comellas-Aragonès, M.; Engelkamp, H.; Claessen, V. I.; Sommerdijk, N. A. J. M.; Rowan, A. E.; Christianen, P. C. M.; Maan, J. C.; Verduin, N. J. M.; Cornelissen, J. L. M.; Nolte, R. J. M. A Virus-Based Single-Enzyme Nanoreactor. *Nat. Nanotechnol.* **2007**, *2*, 635–639.
5. Carette, N.; Engelkamp, H.; Akpa, E.; Pierre, S. J.; Cameron, N. R.; Christianen, P. C. M.; Maan, J. C.; Thies, J. C.; Weberskirch, R.; Rowan, A. E.; et al. A Virus-Based Biocatalyst. *Nat. Nanotechnol.* **2007**, *2*, 226–229.
6. Cardinale, D.; Carette, N.; Michon, T. Virus Scaffolds as Enzyme Nano-carriers. *Trends Biotechnol.* **2012**, *30*, 369–376.
7. Steinmetz, N. F.; Evans, D. J. Utilisation of Plant Viruses in Bionanotechnology. *Org. Biomol. Chem.* **2007**, *5*, 2891–2902.
8. Smith, M. T.; Hawes, A. K.; Bundy, B. C. Reengineering Viruses and Virus-like Particles through Chemical Functionalization Strategies. *Curr. Opin. Chem. Biol.* **2013**, *24*, 1089–1093.
9. Verdaguer, N.; Garriga, D.; Fita, I. X-ray Crystallography of Viruses. In *Structure and Physics of Viruses: Subcellular Biochemistry*; Mateu, M. G., Ed.; Springer: Dordrecht, The Netherlands, 2013; Vol. 68, pp 117−144.
10. Brenner, S.; Horne, R. W. A Negative Staining Method for High Resolution Electron Microscopy of Viruses. *Biochim. Biophys. Acta* **1959**, *34*, 103–110.
11. Adrian, M. J.; Dubochet, J.; Lepault, J.; McDowall, A. W. Cryoelectron Microscopy of Viruses. *Nature* **1984**, *308*, 32–36.
12. Baker, T. S.; Olson, N. H.; Fuller, S. D. Adding the Third Dimension to Virus Life Cycles: Three-Dimensional Reconstruction of Icosahedral Viruses from Cryo-Electron Micrographs. *Microbiol. Mol. Biol. Rev.* **1999**, *63*, 862–922.
13. Baclayon, M.; Wuite, G. J. L.; Roos, W. H. Imaging and Manipulation of Single Viruses by Atomic Force Microscopy. *Soft Matter* **2010**, *6*, 5273–5285.
14. Kuznetsov, Y. G.; McPherson, A. Atomic Force Microscopy in Imaging of Viruses and Virus-Infected Cells. *Microbiol. Mol. Biol. Rev.* **2011**, *75*, 268–285.
15. Martinez-Martin, D.; Carrasco, C.; Hernando-Perez, M.; de Pablo, P. J.; Gomez-Herrero, J.; Perez, R.; Mateu, M. G.; Carrascosa, J. L.; Kiracofe, D.; Melcher, J.; et al. Resolving Structure and Mechanical Properties at the Nanoscale of Viruses with Frequency Modulation Atomic Force Microscopy. *PLoS One* **2012**, *7*, e30204.
16. Kuznetsov, Y. G.; Chang, S.-C.; McPherson, A. Investigation of Bacteriophage T4 by Atomic Force Microscopy. *Bacteriophage* **2011**, *1*, 165–173.
17. Torrance, L.; Andreev, I. A.; Gabrenaite-Verhovskaya, R.; Cowan, G.; Mäkinen, K.; Taliansky, M. E. An Unusual Structure at One End of Potato Potyvirus Particles. *J. Mol. Biol.* **2006**, *357*, 1–8.
18. Obraztsova, E. A.; Kalinina, N. O.; Taliansky, M. E.; Gabrenaite-Verkhovskaya, R.; Mäkinen, K.; Yaminsky, I. V. Atomic Force Microscopy of Potato Virus A. *Colloid J.* **2008**, *70*, 199–201.
19. Kiselyova, O. I.; Yaminsky, I. V.; Karpova, O. V.; Rodionova, N. P.; Kozlovsky, S. V.; Arkhipenko, M. V.; Atabekov, J. G. AFM Study of Potato Virus X Disassembly Induced by Movement Protein. *J. Mol. Biol.* **2003**, *332*, 321–325.
20. Roosa, W. H.; Radtkeb, K.; Kniesmeijera, E.; Geertsemaa, H.; Sodeikb, B.; Wuite, G. J. L. Scaffold Expulsion and Genome Packaging Trigger Stabilization of Herpes Simplex Virus Capsids. *Proc. Natl. Acad. Sci. U.S.A.* **2009**, *106*, 9673–9678.
21. Miller, R. A.; Presley, A. D.; Francis, M. B. Self-Assembling Light-Harvesting Systems from Synthetically Modified Tobacco Mosaic Virus Coat Proteins. *J. Am. Chem. Soc.* **2007**, *129*, 3104–3109.

22. Endo, M.; Fujitsuka, M.; Majima, T. Porphyrin Light-Harvesting Arrays Constructed in the Recombinant Tobacco Mosaic Virus Scaffold. *Chem.—Eur. J.* **2007**, *13*, 8660–8666.
23. Nam, Y. S.; Magyar, A. P.; Lee, D.; Kim, J.-W.; Yun, D. S.; Park, H.; Pollom, T. S., Jr.; Weitz, D. A.; Belcher, A. M. Biologically Templated Photocatalytic Nanostructures for Sustained Light-Driven Water Oxidation. *Nat. Nanotechnol.* **2010**, *5*, 340–344.
24. Steinmetz, N. F.; Lomonossoff, G. P.; Evans, D. J. Cowpea Mosaic Virus for Material Fabrication: Addressable Carboxylate Groups on a Programmable Nanoscaffold. *Langmuir* **2006**, *22*, 3488–3490.
25. Steinmetz, N. F.; Lomonossoff, G. P.; Evans, D. J. Decoration of Cowpea Mosaic Virus with Multiple, Redox-Active, Organometallic Complexes. *Small* **2006**, *2*, 530–533.
26. Cialla, D.; Deckert-Gaudig, T.; Budich, C.; Laue, M.; Möller, R.; Naumann, D.; Deckert, V.; Popp, J. Raman to the Limit: Tip-Enhanced Raman Spectroscopic Investigations of a Single Tobacco Mosaic Virus. *J. Raman Spectrosc.* **2009**, *40*, 240–243.
27. Hermann, P.; Hermelink, A.; Lausch, V.; Holland, G.; Möller, L.; Bannert, N.; Naumann, D. Evaluation of Tip-Enhanced Raman Spectroscopy for Characterizing Different Virus Strains. *Analyst* **2011**, *136*, 1148–1152.
28. Brehm, M.; Taubner, T.; Hillenbrand, R.; Keilmann, F. Infrared Spectroscopic Mapping of Single Nanoparticles and Viruses at Nanoscale Resolution. *Nano Lett.* **2006**, *6*, 1307–1310.
29. Amenabar, I.; Poly, S.; Nuansing, W.; Hubrich, E. H.; Govyadinov, A. A.; Huth, F.; Krutokhvostov, R.; Zhang, L.; Knez, M.; Heberle, J.; et al. Structural Analysis and Mapping of Individual Protein Complexes by Infrared Nanospectroscopy. *Nat. Commun.* **2013**, *4*, 2890.
30. Macpherson, J. V.; Unwin, P. R. Combined Scanning Electrochemical−Atomic Force Microscopy. *Anal. Chem.* **2000**, *72*, 276–285.
31. Kranz, C.; Friedbacher, G.; Mizaikoff, B.; Lugstein, A.; Smoliner, J.; Bertagnolli, E. Integrating an Ultramicroelectrode in an AFM Cantilever. Combined Technology for Enhanced Information. *Anal. Chem.* **2001**, *73*, 2491–2500.
32. Eifert, A.; Kranz, C. Hyphenating Atomic Force Microscopy. *Anal. Chem.* **2014**, *86*, 5190–5200.
33. Bard, A. J. Introduction and Principles. In *Scanning Electrochemical Microscopy*, 2nd ed.; Bard, A. J., Mirkin, M. V., Eds.; Marcel Dekker: New York, 2012; pp 1−14.
34. Wittstock, G.; Burchardt, M.; Pust, E. S.; Shen, Y.; Zhao, C. Scanning Electrochemical Microscopy for Direct Imaging of Reaction Rates. *Angew. Chem., Int. Ed.* **2007**, *46*, 1584–1617.
35. Horrocks, B. R.; Wittstock, G. Biotechnological Applications. In *Scanning Electrochemical Microscopy*, 2nd ed.; Bard, A. J., Mirkin, M. V., Eds.; Marcel Dekker: New York, 2012; pp 317−378.
36. Fan, F.-R. F. Scanning Electrochemical Microscopic Imaging. In *Scanning Electrochemical Microscopy*, 2nd ed.; Bard, A. J., Mirkin, M. V., Eds.; Marcel Dekker: New York, 2012; pp 53−74.
37. Shao, Y.; Mirkin, M. V.; Fish, G.; Kokotov, S.; Palanker, D.; Lewis, A. Nanometer-Sized Electrochemical Sensors. *Anal. Chem.* **1997**, *69*, 1627–1634.
38. Laforge, F. O.; Velmurugan, J.; Wang, Y.; Mirkin, M. V. Nanoscale Imaging of Surface Topography and Reactivity with the Scanning Electrochemical Microscope. *Anal. Chem.* **2009**, *81*, 3143–3150.
39. Mauzeroll, J.; Schougaard, S. B. Scanning Electrochemical Microscopy of Living Cells. In *Scanning Electrochemical Microscopy*, 2nd ed.; Bard, A. J., Mirkin, M. V., Eds.; Marcel Dekker: New York, 2012; pp 379−415.
40. Fan, F.-R. F.; Bard, A. J. Imaging of Biological Macromolecules on Mica in Humid Air by Scanning Electrochemical Microscopy. *Proc. Natl. Acad. Sci. U.S.A.* **1999**, *96*, 14222–14227.
41. Kranz, C. Recent Advancements in Nanoelectrodes and Nanopipettes Used in Combined Scanning Eectrochemical Microscopy Techniques. *Analyst* **2014**, *139*, 336–352.
42. Takahashi, Y.; Shevchuk, A. I.; Novak, P.; Zhang, Y.; Ebejer, N.; Macpherson, J. V.; Unwin, P. R.; Pollard, A. J.; Roy, D.; Clifford, C. A.; et al. Multifunctional Nanoprobes for Nanoscale Chemical Imaging and Localized Chemical Delivery at Surfaces and Interfaces. *Angew. Chem., Int. Ed.* **2011**, *50*, 9638–9642.
43. Actis, P.; Tokar, S.; Clausmeyer, J.; Babakinejad, B.; Mikhaleva, S.; Cornut, R.; Takahashi, Y.; López Córdoba, A.; Novak, P.; Shevchuck, A. I.; et al. Electrochemical Nanoprobes for Single-Cell Analysis. *ACS Nano* **2014**, *8*, 875–884.
44. Takahashi, Y.; Shevchuk, A. I.; Novak, P.; Babakinejad, B.; Macpherson, J.; Unwin, P. R.; Shiku, H.; Gorelik, J.; Klenerman, D.; Korchev, Y. E.; et al. Topographical and Electrochemical Nanoscale Imaging of Living Cells using Voltage-Switching Mode Scanning Electrochemical Microscopy. *Proc. Natl. Acad. Sci. U.S.A.* **2012**, *109*, 11540–11545.
45. Takahashi, Y.; Shevchuk, A. I.; Novak, P.; Murakami, Y.; Shiku, H.; Korchev, Y. E.; Matsue, T. Simultaneous Noncontact Topography and Electrochemical Imaging by SECM/SICM Featuring Ion Current Feedback Regulation. *J. Am. Chem. Soc.* **2010**, *132*, 10118–10126.
46. Ebejer, N.; Schnippering, M.; Colburn, A. W.; Edwards, M. A.; Unwin, P. R. Localized High Resolution Electrochemistry and Multifunctional Imaging: Scanning Electrochemical Cell Microscopy. *Anal. Chem.* **2010**, *82*, 9141–9145.
47. Abbou, J.; Anne, A.; Demaille, C. Probing the Structure and Dynamics of End-Grafted Flexible Polymer Chain Layers by Combined Atomic Force−Electrochemical Microscopy. Cyclic Voltammetry within Nanometer-Thick Macromolecular Poly(ethylene glycol) Layers. *J. Am. Chem. Soc.* **2004**, *126*, 10095–10108.
48. Abbou, J.; Anne, A.; Demaille, C. Accessing the Dynamics of End-Grafted Flexible Polymer Chains by Atomic Force-Electrochemical Microscopy. Theoretical Modeling of the Approach Curves by the Elastic Bounded Diffusion Model and Monte Carlo Simulations. Evidence for Compression-Induced Lateral Chain Escape. *J. Phys. Chem. B* **2006**, *110*, 22664–22675.
49. Anne, A.; Cambril, E.; Chovin, A.; Demaille, C. Touching Surface-Attached Molecules with a Microelectrode: Mapping the Distribution of Redox-Labeled Macromolecules by Electrochemical−Atomic Force Microscopy. *Anal. Chem.* **2010**, *82*, 6353–6362.
50. Wang, K.; Goyer, C.; Anne, A.; Demaille, C. Exploring the Motional Dynamics of End-Grafted DNA Oligonucleotides by *In-Situ* Electrochemical Atomic Force Microscopy. *J. Phys. Chem. B* **2007**, *111*, 6051–6058.
51. Huang, K.; Anne, A.; Bahri, M. A.; Demaille, C. Probing Individual Redox PEGylated Gold Nanoparticles by Electrochemical−Atomic Force Microscopy. *ACS Nano* **2013**, *7*, 4151–4163.
52. Anne, A.; Chovin, A.; Demaille, C.; Lafouresse, M. High-Resolution Mapping of Redox-Immunomarked Proteins Using Electrochemical Atomic Force Microscopy in Molecule Touching Mode. *Anal. Chem.* **2011**, *83*, 7924–7932.
53. Huang, Y.; Chiang, C. Y.; Lee, S. K.; Gao, Y.; Hu, E.; De Yoreo, J.; Belcher, A. M. Programmable Assembly of Nanoarchitectures Using Genetically Engineered Viruses. *Nano Lett.* **2005**, *5*, 1429–1434.
54. Moghal, S. M.; Francki, R. I. Towards a System for the Identification and Classification of Potyviruses. II. Virus Particle Length, Symptomatology, and Cytopathology of Six Distinct Viruses. *Virology* **1981**, *112*, 210–216.
55. Brandes, J.; Wetter, C. Classification of Elongated Plant Viruses on the Basis of Particle Morphology. *Virology* **1959**, *8*, 99–115.
56. Kendall, A.; McDonald, M.; Bian, W.; Bowles, T.; Baumgarten, S. C.; Shi, J.; Stewart, P. L.; Bullitt, E.; Gore, D.; Irving, T. C.; et al. Structure of Flexible Filamentous Plant Viruses. *J. Virol.* **2008**, *82*, 9546–9554.
57. Murphy, J. F.; Rychlik, W.; Rhoads, R. E.; Hunt, A. G.; Shaw, J. G. A Tyrosine Residue in the Small Nuclear Inclusion Protein of Tobacco Vein Mottling Virus Links the VPg to the Viral RNA. *J. Virol.* **1991**, *65*, 511–513.

58. Puustinen, P.; Rajamäki, M.-L.; Ivanov, K. I.; Valkonen, J. P. T.; Mäkinen, K. Detection of the Potyviral Genome-Linked Protein VPg in Virions and Its Phosphorylation by Host Kinases. *J. Virol.* **2002**, *76*, 12703–12711.
59. Gabrenaite-Verkhovskaya, R.; Andreev, I. A.; Kalinina, N. O.; Torrance, L.; Taliansky, M. E.; Mäkinen, K. Cylindrical Inclusion Protein of Potato Virus A Is Associated with a Subpopulation of Particles Isolated from Infected Plants. *J. Gen. Virol.* **2008**, *89*, 829–838.
60. Hegner, M.; Wagner, P.; Semenza, G. Ultralarge Atomically Flat Template-Stripped Au Surfaces for Scanning Probe Microscopy. *Surf. Sci.* **1993**, *291*, 39–46.
61. Anne, A.; Demaille, C.; Moiroux, J. Elastic Bounded Diffusion. Dynamics of Ferrocene-Labeled Poly(ethylene glycol) Chains Terminally Attached to the Outermost Monolayer of Successively Self-Assembled Monolayers of Immunoglobulins. *J. Am. Chem. Soc.* **1999**, *121*, 10379–10388.
62. Smith, R. L.; Rohrer, G. S. The Preparation of Tip and Sample for Scanning Probe Experiments. In *Scanning Probe Microscopy and Spectroscopy: Theory, Techniques and Applications*, 2nd ed.; Bonnell, D., Ed.; Wiley-VCH: New York, 2001; pp 155−201.
63. San Paulo, A.; García, R. High-Resolution Imaging of Antibodies by Tapping-Mode Atomic Force Microscopy: Attractive and Repulsive Tip−Sample Interaction Regimes. *Biophys. J.* **2000**, *78*, 1599–1605.
64. Knez, M.; Sumser, M. P.; Bittner, A. M.; Wege, C.; Jeske, H.; Hoffmann, D. M. P.; Kuhnke, K.; Kern, K. Binding the Tobacco Mosaic Virus to Inorganic Surfaces. *Langmuir* **2004**, *20*, 441–447.
65. Xu, X.; Carrasco, C.; de Pablo, P. J.; Gomez-Herrero, J.; Raman, A. Unmasking Imaging Forces on Soft Biological Samples in Liquids When Using Dynamic Atomic Force Microscopy: A Case Study on Viral Capsids. *Biophys. J.* **2008**, *95*, 2520–2528.
66. Płochocka, D.; Wełnicki, M.; Zielenkiewicz, P.; Ostoja-Zagórski, W. Three-Dimensional Model of the Potyviral Genome-Linked Protein. *Proc. Natl. Acad. Sci. U.S.A.* **1996**, *93*, 12150–12154.
67. Lamy, J.; Lamy, J.; Billiald, P.; Sizaret, P. Y.; Cave, G.; Frank, J.; Motta, G. Approach to the Direct Intramolecular Localization of Antigenic Determinants in *Androctonus australis* Hemocyanin with Monoclonal Antibodies by Molecular Immunoelectron Microscopy. *Biochemistry* **1985**, *24*, 5532–5542.
68. Fan, F.-R. F.; Bard, A. J. Electrochemical Detection of Single Molecules. *Science* **1995**, *267*, 871–874.
69. Fan, F.-R. F.; Juhyoun Kwak, J.; Bard, A. J. Single Molecule Electrochemistry. *J. Am. Chem. Soc.* **1996**, *118*, 9669–9675.
70. Sun, P.; Mirkin, M. V. Electrochemistry of Individual Molecules in Zeptoliter Volumes. *J. Am. Chem. Soc.* **2008**, *130*, 8241–8250.
71. Anne, A.; Moiroux, J. Quantitative Characterization of the Flexibility of Poly(ethylene glycol) Chains Attached to a Glassy Carbon Electrode. *Macromolecules* **1999**, *32*, 5829–5835.
72. Kuznetsov, Y. G.; Chang, S.-C.; McPherson, A. Investigation of Bacteriophage T4 by Atomic Force Microscopy. *Bacteriophage* **2011**, *1*, 165–173.
73. Macpherson, J. V.; Unwin, P. R. Combined Scanning Electrochemical−Atomic Force Microscopy. *Anal. Chem.* **2000**, *72*, 276–285.
74. Abbou, J.; Demaille, C.; Druet, M.; Moiroux, J. Fabrication of Submicrometer-Sized Gold Electrodes of Controlled Geometry for Scanning Electrochemical−Atomic Force Microscopy. *Anal. Chem.* **2002**, *74*, 6355–6363.
75. Ives, D. J. G.; Janz, G. J. *References Electrodes*; Academic: New York, 1961.
76. Horcas, I.; Fernández, R.; Gómez-Rodríguez, J. M.; Colchero, J.; Gómez-Herrero, J.; Baro, A. M. WSxM: A Software for Scanning Probe Microscopy and a Tool for Nanotechnology. *Rev. Sci. Instrum.* **2007**, *78*, 013705.